Generalized Gradient Vector Flow for Snakes: New Observations, Analysis, and Improvement

Lunming Qin, Ce Zhu, *Senior Member, IEEE,* Yao Zhao, *Senior Member, IEEE,* Huihui Bai, and Huawei Tian

***Abstract*—Snakes, or active contours, have been widely used in image processing applications. An external force for snakes called gradient vector flow (GVF) attempts to address traditional snake problems of initialization sensitivity and poor convergence to concavities, while generalized GVF (GGVF) aims to improve GVF snake convergence to long and thin indentations (LTIs). In this paper, we find and show that both GVF and GGVF snakes essentially yield the same performance in capturing LTIs of odd widths, and generally neither can converge to even-width LTIs. Based on a thorough investigation of the GVF and GGVF fields within the LTI during their iterative processes, we identify the crux of the convergence problem, and accordingly propose a novel external force termed as component-normalized GGVF (CN-GGVF) to eliminate the problem. CN-GGVF is obtained by normalizing each component of initial GGVF vectors with respect to its own magnitude. Experimental results and comparisons against GGVF snakes show that the proposed CN-GGVF snakes can capture LTIs regardless of odd or even widths with a remarkably faster convergence speed, while preserving other desirable properties of GGVF snakes with lower computational complexity in vector normalization.**

***Index Terms*—Active contour models, convergence, external force, gradient vector flow (GVF), snakes.**

I. Introduction

SINCE SNAKES, or active contours, were first proposed by Kass *et al.* [1] in 1987, they have become one of the most active and successful research areas in computer vision and image processing applications [2]. Active contours are curves defined within an image domain that deform under the influence of internal and external forces to conform to desired features (like edges). Internal forces defined within the curve itself are determined by the geometric properties of the curve, while external forces are derived from the image data, which have been the most discussed issue in active contour models.

An energy function associated with the curve is defined, so that the problem of finding desired features is converted into an energy minimization process. Due to its high efficiency, the snake model has found many applications, including edge detection [1], shape recovery [3], [4], object tracking [5]–[8], and image segmentation [9]–[12]. However, there are two key shortcomings with the traditional snake. First, the initial contour must be close enough to the desired features, otherwise the snake will likely converge to a wrong result. Second, it is difficult for the snake to move into boundary concavities [13], [14].

An external force for snakes, called gradient vector flow (GVF) [15], was introduced to largely overcome the two limitations of the traditional snake. GVF is computed as a diffusion of the gradient vectors of a gray-level or binary edge map derived from an image. Since its publication about a decade ago, GVF has been widely used and adapted to various models and problems, e.g., segmentation [16]–[19], tracking [6], [8], registration [20], and skeletonization [21]. Additionally, automatic initialization methods of the GVF snake can be found in [22] and [23]. Efficient numerical schemes are applied to speed up the GVF computation [24], [25].

Although GVF has been widely used and improved in various models, it still exhibits some defects, such as the difficulty in forcing a snake into long and thin indentations (LTIs) as well as noise sensitivity. In [26], Xu and Prince proposed a generalized version of GVF (generalized GVF or GGVF) by introducing two spatially varying weighting functions, which has been reported to improve GVF convergence to LTIs as well as robustness to noise. In [27], the GVF in the normal direction (NGVF) snake is proposed, which can enter into LTIs at a faster convergence speed. Furthermore, the normally biased GVF (NBGVF) snake is claimed to perform well on weak edge preserving and noise robustness while maintaining the desirable properties of capturing LTIs [28]. In [29], by adding a new external force, an improved GVF active contour is presented to detect LTIs. Besides these general snakes, there are also some specific active contours aiming to segment the narrow structures, like blood vessels in medical data or roads in aerial images [30], [31]. In spite of the various improvements for GVF/GGVF, the underlying mechanism for the difficulty in capturing LTIs has still not been fully understood.

In this paper, we revisit the conventional edge-based parametric GVF and GGVF snakes to present some new

Manuscript received April 7, 2012; revised September 3, 2012; accepted October 17, 2012. Date of publication January 24, 2013; date of current version May 1, 2013. This work was supported in part by the 973 Program, under Grant 2012CB316400; the National Natural Science Funds for Distinguished Young Scholar, under Grant 61025013; the National NSF of China, under Grant 61210006, Grant 61202240, Grant 60903066, Grant 61272051, and Grant 61201393. This paper was recommended by Associate Editor H. Wang.

L. Qin, H. Bai, and H. Tian are with the Institute of Information Science, Beijing Jiaotong University, Beijing Key Laboratory of Advanced Information Science and Network Technology, Beijing 100044, China (e-mail: lunming.qin@hotmail.com; hhbai@bjtu.edu.cn; hwtian@live.cn).

C. Zhu is with the School of Electronic Engineering, University of Electronic Science and Technology of China, Chengdu 611731, China (e-mail: eczhu@uestc.edu.cn).

Y. Zhao is with the Institute of Information Science, Beijing Jiaotong University, and with the State Key Laboratory of Rail Traffic Control and Safety, Beijing 100044, China (e-mail: yzhao@bjtu.edu.cn).

Color versions of one or more of the figures in this paper are available online at http://ieeexplore.ieee.org.

Digital Object Identifier 10.1109/TCSVT.2013.2242554

observations and the associated analysis, and then identify the intrinsic difficulties with respect to GVF and GGVF convergence to LTIs. Based on the theoretical analysis we propose an improved snake model. Specifically, our main contributions are summarized as follows.

1) New observations on GVF and GGVF snakes are given to show that the two models essentially yield the same performance in capturing LTIs of odd widths, and generally neither can converge to even-width LTIs. The observations are different from the opinion in [26] that GGVF snakes outperform GVF snakes in the convergence to LTIs.
2) The force characteristics within LTIs are theoretically investigated, based on which, we identify two intrinsic difficulties for GVF and GGVF snakes in convergence to LTIs, namely, the obliteration and noise problems. More details on the theoretical analysis and the two problems can be found in Sections III and IV, respectively.
3) To cope with the obliteration problem, a simple yet effective external force called component-normalized GGVF (CN-GGVF) is developed, which can efficiently move the snake into even-width LTIs, with details in Section V.

The remainder of the paper is organized as follows. Section II reviews the traditional snake, GVF and GGVF snakes, and presents some new observations. Section III theoretically examines the force characteristics within LTIs and Section IV identifies the two intrinsic difficulties in convergence to LTIs, i.e., the obliteration and noise problems, in GVF and GGVF. In Section V, a novel external force termed CN-GGVF for snakes is proposed. Furthermore, performance of the CN-GGVF snake is examined in Section VI and the conclusion is given in Section VII.

II. Background and New Observations

A. Traditional Snake Model

The traditional snake is represented by a parametric curve $\mathbf{c}(s) = [x(s), y(s)]$, $s \in [0, 1]$, which deforms through the spatial domain of an image to minimize the energy function [1]

$$E(\mathbf{c}(s)) = \int_0^1 \left[\frac{1}{2}(\alpha\left|\mathbf{c}'(s)\right|^2 + \beta\left|\mathbf{c}''(s)\right|^2) + E_{\text{ext}}(\mathbf{c}(s))\right] ds \quad (1)$$

where α and β are weighting parameters controlling the snake's tension and rigidity, respectively, and $\mathbf{c}'(s)$ and $\mathbf{c}''(s)$ are the first and second derivatives of $\mathbf{c}(s)$ with respect to s. The first two terms within the above integral stand for the internal energy. The external energy $E_{\text{ext}}(\mathbf{c}(s))$ derived from the image data takes on its smaller values at the desired features. Representative external energy functions for a gray-level image $I(x, y)$ for seeking step edges are given as [1]

$$E_{\text{ext}}^{(1)}(x, y) = -|\nabla I(x, y)|^2 \quad (2)$$

$$E_{\text{ext}}^{(2)}(x, y) = -|\nabla[G_\sigma(x, y) * I(x, y)]|^2 \quad (3)$$

where $G_\sigma(x, y)$ is a 2-D Gaussian function with standard deviation σ, $*$ denotes linear convolution, and ∇ is the gradient operator. Typical external energy functions for a line-drawing (black on white) [32] are

$$E_{\text{ext}}^{(3)}(x, y) = I(x, y) \quad (4)$$

$$E_{\text{ext}}^{(4)}(x, y) = G_\sigma(x, y) * I(x, y). \quad (5)$$

To minimize $E(\mathbf{c}(s))$, the snake must satisfy the Euler–Lagrange equation

$$\alpha\mathbf{c}''(s) - \beta\mathbf{c}''''(s) - \nabla E_{\text{ext}}(\mathbf{c}(s)) = 0 \quad (6)$$

which can be viewed as a force balance equation

$$F_{\text{int}}(\mathbf{c}(s)) + F_{\text{ext}}(\mathbf{c}(s)) = 0 \quad (7)$$

where $F_{\text{int}}(\mathbf{c}(s)) = \alpha\mathbf{c}''(s) - \beta\mathbf{c}''''(s)$ is the internal force shrinking and smoothing the contour, and the external force $F_{\text{ext}}(\mathbf{c}(s)) = -\nabla E_{\text{ext}}(\mathbf{c}(s))$ pulls the snake to the desired features.

To find a solution to (6), the active contour $\mathbf{c}(s)$ has to evolve dynamically as a function of time t, i.e., $\mathbf{c}(s, t)$. By making the partial derivative of $\mathbf{c}(s, t)$ with respect to t, i.e., $\mathbf{c}_t(s, t)$, equal to the left-hand side of (6), the dynamic snake function is given as

$$\mathbf{c}_t(s, t) = \alpha\mathbf{c}''(s, t) - \beta\mathbf{c}''''(s, t) - \nabla E_{\text{ext}}(\mathbf{c}(s, t)). \quad (8)$$

The solution $\mathbf{c}(s)$ of (6) is obtained when the steady-state solution $\mathbf{c}(s, t)$ of (8) is reached ($\mathbf{c}_t(s, t) = 0$) from an initial contour $\mathbf{c}(s, 0)$. A numerical solution of $\mathbf{c}(s, t)$ on a discrete grid can be obtained by discretizing (8) and solving the discrete equation iteratively [1], [33].

B. GVF Snake Model

Xu and Prince proposed gradient vector flow (GVF) [15] as an external force for active contours to largely overcome the two key shortcomings of the traditional snake. The force balance equation (7) is used as a starting point for designing a GVF snake. The external force term $-\nabla E_{\text{ext}}(\mathbf{c}(s))$ in (7) is replaced with a GVF field $\mathbf{v}(x, y) = [u(x, y), v(x, y)]$ defined as the equilibrium solution of the following vector partial differential equation:

$$\mathbf{v}_t(x, y, t) = \mu\nabla^2\mathbf{v}(x, y, t) - |\nabla f|^2\left[\mathbf{v}(x, y, t) - \nabla f\right] \quad (9)$$

where $\mathbf{v}_t(x, y, t)$ is the partial derivative of $\mathbf{v}(x, y, t)$ with respect to t, and $\nabla^2 = \partial^2/\partial x^2 + \partial^2/\partial y^2$ denotes the Laplacian operator. f is an edge map derived from the image and defined to have larger values at the desired features, which is typically the additive inverse of an external energy function as given in (2)–(5). μ controls the smoothness degree of the GVF field and should be set according to the noise level in the image (larger μ for more noise).

C. GGVF Snake Model

1) *GGVF Field:* By introducing two spatially varying weighting functions into the GVF formulation, Xu and Prince proposed an external force referred to as generalized gradient vector flow (GGVF) [26]. As a generalization of GVF, GGVF was reported to improve contour convergence to LTIs and

robustness to noise, which is defined as the equilibrium solution of the following partial differential equation:

$$\mathbf{v}_t(x, y, t) = g(|\nabla f|)\nabla^2\mathbf{v}(x, y, t) - h(|\nabla f|)[\mathbf{v}(x, y, t) - \nabla f] \tag{10}$$

where

$$g(|\nabla f|) = \exp(-|\nabla f|/k) \tag{11}$$

$$h(|\nabla f|) = 1 - \exp(-|\nabla f|/k). \tag{12}$$

The parameter k regulates to some extent the tradeoff between the first term (known as smoothing term) and the second term (known as data term) in the right-hand side of (10) and it should be set according to the amount of noise in the image (larger k for higher noise levels).

2) *Numerical Implementation:* As in [26], the partial differential equation (10) specifying the GGVF field can be implemented using an explicit finite difference scheme. In (10), $|\nabla f|$ can be calculated using any digital image gradient operator, e.g., simple central differences employed in this paper. Since the data term in (10) is defined to encourage the GGVF field to be close to the edge map gradient computed from the image, its weighting coefficient $h(|\nabla f|)$ must be greater than or equal to 0. According to (12), the parameter k must be greater than 0.

To set up the iterative solution, let the spatial sample intervals be Δx and Δy and the time step for each iteration be Δt. The partial derivative $\mathbf{v}_t(x, y, t)$ can then be approximated as $[\mathbf{v}(x, y, t + \Delta t) - \mathbf{v}(x, y, t)]/\Delta t$. On a discrete grid, the Laplacian term can be approximated by

$$\nabla^2\mathbf{v}(x, y, t) = \frac{1}{\Delta x \Delta y}\mathbf{A} * \mathbf{v}(x, y, t) \tag{13}$$

where $\mathbf{A} = \begin{bmatrix} 0 & 1 & 0 \\ 1 & -4 & 1 \\ 0 & 1 & 0 \end{bmatrix}$ is the Laplacian matrix.

Substituting the above approximations into (10) gives an iterative solution to the GGVF field as follows:

$$\begin{aligned}\mathbf{v}(x, y, t + \Delta t) = {} & \mathbf{v}(x, y, t) + \tfrac{\Delta t}{\Delta x \Delta y} g(|\nabla f|)\,\mathbf{A} * \mathbf{v}(x, y, t) \\ & - \Delta t h(|\nabla f|)[\mathbf{v}(x, y, t) - \nabla f].\end{aligned} \tag{14}$$

According to the GGVF stability constraint $\Delta t/(\Delta x \Delta y) \leq 1/4$ [26], Δt must be not larger than $1/4$ by making $\Delta x = \Delta y = 1$. To obtain the maximum smoothness of the GGVF field, we set $\Delta t = 1/4$. Accordingly, (14) can be rewritten as

$$\begin{aligned}\mathbf{v}(x, y, t + \Delta t) = {} & \mathbf{v}(x, y, t) + \tfrac{1}{4} g(|\nabla f|)\,\mathbf{A} * \mathbf{v}(x, y, t) \\ & - \tfrac{1}{4} h(|\nabla f|)[\mathbf{v}(x, y, t) - \nabla f].\end{aligned} \tag{15}$$

The desired external force field $\mathbf{v}(x, y, t)$ is iteratively calculated from the initial vector field $\mathbf{v}(x, y, 0) = \nabla f$, i.e., the gradient of the edge map. Typically, the iteration number (denoted as n) required to calculate the GGVF field or the above GVF field for an $n_1 \times n_2$-pixel image is $\sqrt{n_1 \times n_2}$ [15].

After the iterative process, external forces in actual implementations are normalized to unit vectors to make the snake evolve at a constant speed. Typically, the initial GGVF vectors $\mathbf{v}(x, y) = [u(x, y), v(x, y)]$ are normalized with respect to their magnitudes using

$$\mathbf{v}_{\text{vn-ggvf}}(x, y) = \begin{cases} \mathbf{v}(x, y)/|\mathbf{v}(x, y)|, & |\mathbf{v}(x, y)| \neq 0 \\ [0, 0], & |\mathbf{v}(x, y)| = 0 \end{cases} \tag{16}$$

which is referred to as vector-based normalization.

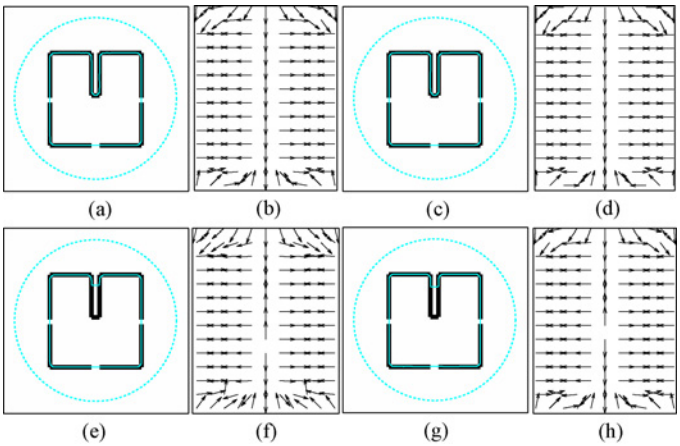

Fig. 1. Performance of GVF and GGVF snakes in detecting an odd-width LTI. The initial and resulting snakes are indicated by cyan dashed and solid lines, respectively. The external force fields in the top and bottom rows are properly and over smoothed, respectively. First column: GVF snakes. Second column: GVF fields within the LTI. Third column: GGVF snakes. Fourth column: GGVF fields within the LTI. (a) GVF snake. (b) Properly smoothed. (c) GGVF snake. (d) Properly smoothed. (e) GVF snake. (f) Over-smoothed. (g) GGVF snake. (h) Over-smoothed.

D. New Observations on GVF and GGVF Snakes

It was reported in [26] that GGVF snakes outperform GVF snakes in the convergence to LTIs. GVF's difficulty of forcing a snake into an LTI is caused by excessive smoothing of the field near the LTI boundary, governed by the smoothing coefficient μ in (9). When a much smaller μ is used, the GVF snake can also achieve a good convergence to the LTI similar to that of GGVF, but at the expense of an order of magnitude higher computational complexity than that of GGVF [26].

However, to our observation, GVF and GGVF snakes yield almost the same performance in convergence to LTIs. Specifically, when the LTI width is of an odd number of pixels, both snakes can converge completely to the LTI if their external force fields are appropriately smoothed[1], as reported in [26], whereas the computational cost required for the GVF field is almost the same as that for the GGVF field, which is opposed to the opinion in [26]. However, if their vector fields are over-smoothed[2], not only the GVF snake but also the GGVF snake fails to capture the LTI. On the other hand, when the LTI width is an even number of pixels, in general, neither the GVF snake nor the GGVF snake is able to detect the LTI no matter how their external force fields are smoothed. The following will further elaborate our observations.

Fig. 1 shows the performance of the GVF and GGVF snakes in capturing an odd-width LTI. The original image in Fig. 1 is a line-drawing of a square-shaped object (shown in black) with the odd-width LTI. All resulting snakes indicated by cyan solid lines are derived from a same initialization indicated by a cyan dashed line. All fields within the LTI are sampled by a factor of 3 in the y direction. We find that at almost the same computational cost, both the GVF snake in Fig. 1(a)

[1]The vector field is considered to be appropriately smoothed when k in (10) is less than a selected value to be discussed in Section IV-B.

[2]The vector field is considered to be over-smoothed when k is greater than the selected value.

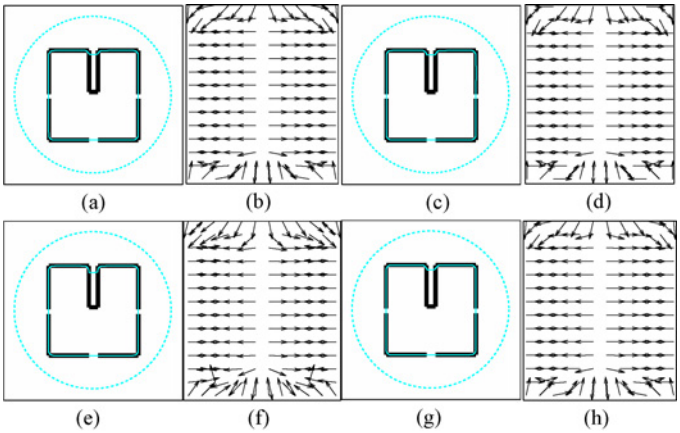

Fig. 2. Performance of GVF and GGVF snakes in detecting an even-width LTI. The initial and resulting snakes are indicated by cyan dashed and solid lines, respectively. The external force fields in the top and bottom rows are properly and over smoothed, respectively. First column: GVF snakes. Second column: GVF fields within the LTI. Third column: GGVF snakes. Fourth column: GGVF fields within the LTI. (a) GVF snake. (b) Properly smoothed. (c) GGVF snake. (d) Properly smoothed. (e) GVF snake. (f) Over-smoothed. (g) GGVF snake. (h) Over-smoothed.

and the GGVF snake in Fig. 1(c) converge completely to the odd-width LTI when their vector fields are appropriately smoothed, as shown zoomed in Fig. 1(b) and (d), respectively. On the contrary, if their vector fields are over-smoothed, not only the GVF snake in Fig. 1(e), but also the GGVF snake in Fig. 1(g) is unable to detect the LTI. The corresponding GVF and GGVF fields are shown zoomed in Fig. 1(f) and (h), respectively.

Fig. 2 shows the performance of the GVF and GGVF snakes in capturing an even-width LTI. In Fig. 2, the original image is a line-drawing of a square-shaped object (shown in black) with the even-width LTI. All resulting snakes represented by cyan solid lines are derived from a same initialization represented by a cyan dashed line. All fields within the LTI are sampled by a factor of 3 in the y direction. From Fig. 2, we can observe that neither the GVF snakes in the first column nor the GGVF snakes in the third column are able to move into the even-width LTI whether their vector fields are appropriately or over smoothed. The GVF and GGVF fields are shown zoomed in the second and fourth columns, respectively. In summary, Figs. 1 and 2 demonstrate that GVF and GGVF snakes exhibit almost the same performance in terms of convergence to LTIs regardless of odd or even widths, which is different from the opinion in [26]. More in-depth analyses and validations will be provided in the following section.

III. Analysis of Force Field Characteristics Within LTIs

Since the role of external forces is to attract the snake to the desired boundary, external forces within LTIs are thoroughly investigated in this section to explore the convergence behavior of the GGVF snakes. In this paper, we refer to the gradient vectors of the edge map as diffusion sources for the GVF and GGVF external forces, and the diffusion sources can be further divided into two categories: those at the desired boundaries,

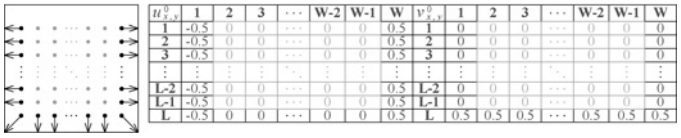

$u^0_{x,y}$	1	2	3	···	W-2	W-1	W	$v^0_{x,y}$	1	2	3	···	W-2	W-1	W
1	-0.5	0	0	···	0	0	0.5	1	0	0	0	···	0	0	0
2	-0.5	0	0	···	0	0	0.5	2	0	0	0	···	0	0	0
3	-0.5	0	0	···	0	0	0.5	3	0	0	0	···	0	0	0
⋮	⋮			⋱			⋮	⋮	⋮			⋱			⋮
L-2	-0.5	0	0	···	0	0	0.5	L-2	0	0	0	···	0	0	0
L-1	-0.5	0	0	···	0	0	0.5	L-1	0	0	0	···	0	0	0
L	-0.5	0	0	···	0	0	0.5	L	0.5	0.5	0.5	···	0.5	0.5	0.5

Fig. 3. Initial external force field with the value of every force component within an $W \times L$-pixel indentation, where gray pixels represent those in the indentation while the black ones are boundary pixels.

and at the nondesired boundaries. Here, the desired boundaries are boundaries of objects we are interested in, while the nondesired boundaries refer to those of other objects or noise.

A. Computational Model for External Forces

Fig. 3 shows an edge map gradient at every pixel within an $W \times L$-pixel indentation. The x- and y-component values of the initial gradient vectors are also listed in Fig. 3. After n ($n = 0, 1, 2, \ldots$) iterations, the external force vector at (x, y) is represented as $\mathbf{v}^n_{x,y} = [u^n_{x,y},\ v^n_{x,y}]$, $x = 1, 2, \ldots, W$, $y = 1, 2, \ldots, L$.

As shown in Fig. 3, for the black pixels at the indentation boundary, we can get $|\nabla f| = 0.5$ or $|\nabla f| = 0.5\sqrt{2}$. To maintain the constant gradient vectors at the indentation boundary during iteration, a small enough smoothing coefficient $g(|\nabla f|)$ and a large enough data coefficient $h(|\nabla f|)$ are required. According to (11) and (12), it would be appropriate to confirm that $g(|\nabla f|) \approx 0$ and $h(|\nabla f|) \approx 1$ with a given small enough $k > 0$. With $g(|\nabla f|) \approx 0$ and $h(|\nabla f|) \approx 1$, (15) becomes

$$\begin{aligned}
&\mathbf{v}(x, y, t + \Delta t)\\
&= \mathbf{v}(x, y, t) + \frac{1}{4} \times 0 \times \mathbf{A} * \mathbf{v}(x, y, t) - \frac{1}{4} \times 1 \times [\mathbf{v}(x, y, t) - \nabla f]\\
&= \mathbf{v}(x, y, t) - \frac{1}{4}[\mathbf{v}(x, y, t) - \nabla f]\\
&= \frac{3}{4}\mathbf{v}(x, y, t) + \frac{1}{4}\nabla f. \qquad (17)
\end{aligned}$$

As $\mathbf{v}(x, y, 0) = \nabla f$, we get

$$\mathbf{v}(x, y, t) = \frac{3}{4}\nabla f + \frac{1}{4}\nabla f = \nabla f. \qquad (18)$$

This means at the black boundary pixels, for $x = 2, 3, \ldots, W - 1$, $\mathbf{v}^n_{x,L} = \mathbf{v}^0_{x,L}$, and for $x = 1, W$, $y = 1, 2, \ldots, L$, $\mathbf{v}^n_{x,y} = \mathbf{v}^0_{x,y}$.

Next, only the external forces at the gray pixels in homogeneous regions, i.e., $\mathbf{v}^n_{x,y}$, $x = 2, 3, \ldots, W - 1$, $y = 1, 2, \ldots, L-1$, are left to be considered. For the gray pixels in Fig. 3, we can get $|\nabla f| = 0$. From (11) and (12), we can obtain $g(|\nabla f|) = 1$ and $h(|\nabla f|) = 0$. By substituting them into (15), the corresponding iterative solution that involves computing GGVF external forces at the gray pixels is obtained as

$$\mathbf{v}(x, y, t + \Delta t) = \mathbf{v}(x, y, t) + \frac{1}{4}\mathbf{A} * \mathbf{v}(x, y, t) \qquad (19)$$

which can be rewritten as

$$\mathbf{v}(x, y, t + \Delta t) = \frac{1}{4}\begin{bmatrix} 0 & 1 & 0 \\ 1 & 0 & 1 \\ 0 & 1 & 0 \end{bmatrix} * \mathbf{v}(x, y, t) \qquad (20)$$

indicating that in homogeneous regions, the value of each component at each pixel is computed as the mean of those

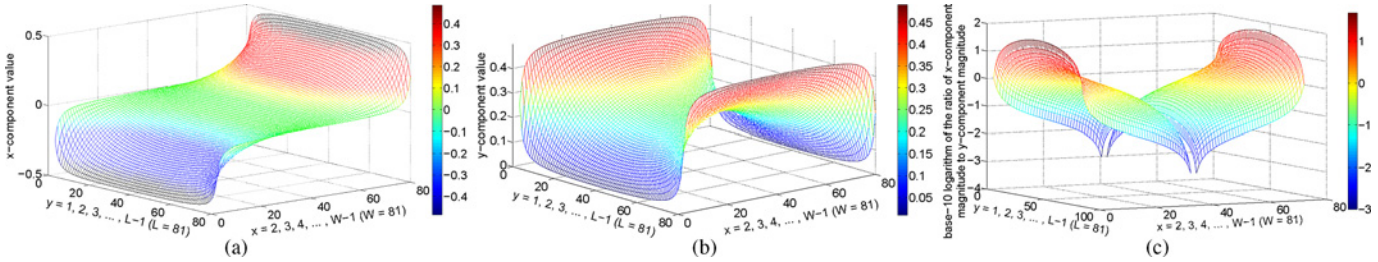

Fig. 4. (a) x- and (b) y-component values of the stabilized external forces at the gray pixels within a 81 × 81-pixel indentation. (c) Base-10 logarithms of the ratios of the x-component magnitudes to the y-component magnitudes.

at its four adjacent pixels after every iteration. Namely, the GGVF external force at each gray pixel (x, y) satisfies

$$\begin{aligned} 4\,\mathbf{v}_{x,y}^{n+1} &= \mathbf{v}_{x-1,y}^{n} + \mathbf{v}_{x,y+1}^{n} + \mathbf{v}_{x+1,y}^{n} + \mathbf{v}_{x,y-1}^{n}, \\ x &= 2, 3, \ldots, W-1, \quad y = 1, 2, \ldots, L-1. \end{aligned} \tag{21}$$

Once the GGVF vector reaches a stable state, we have $\mathbf{v}_{x,y}^{n+1} = \mathbf{v}_{x,y}^{n}$, $x = 2, 3, \ldots, W-1$, $y = 1, 2, \ldots, L-1$. Substituting it into (21) yields a linear equation for each component of the stabilized external force as follows:

$$\begin{aligned} 4\,u_{x,y}^{n} &= u_{x-1,y}^{n} + u_{x,y+1}^{n} + u_{x+1,y}^{n} + u_{x,y-1}^{n}, \\ x &= 2, 3, \ldots, W-1, \quad y = 1, 2, \ldots, L-1 \end{aligned} \tag{22a}$$

$$\begin{aligned} 4\,v_{x,y}^{n} &= v_{x-1,y}^{n} + v_{x,y+1}^{n} + v_{x+1,y}^{n} + v_{x,y-1}^{n}, \\ x &= 2, 3, \ldots, W-1, \quad y = 1, 2, \ldots, L-1. \end{aligned} \tag{22b}$$

Within the $W \times L$-pixel indentation, there are $(W-2)\times(L-1)$ gray pixels corresponding to $(W-2)\times(L-1)$ external force vectors. For given W and L, all the x- and y-component values of the stabilized external forces at the gray pixels are obtained by solving two systems of $(W-2)\times(L-1)$ linear equations, respectively. Note that the pixels enclosing the gray pixels at the top of the indentation are not the boundary pixels as shown in Fig. 3. The external forces at these pixels change as the iteration proceeds according to their iterative solution (20). To solve the two systems of linear equations, we set $\mathbf{v}_{x,0}^{0} = [0, 0.5]$, $x = 2, 3, \ldots, W-1$, such that $\mathbf{v}_{x,0}^{n} = \mathbf{v}_{x,0}^{0} = [0, 0.5]$, $x = 2, 3, \ldots, W-1$, since their iterative solution is changed to (18). Under this assumption, the y-component magnitudes of the stabilized vectors at the gray pixels increase, and the x-component magnitudes decrease according to (18) and (20).

B. Analysis on Force Field Characteristics

An example of solving the above systems of linear equations with $W = 81$ and $L = 81$ of an odd-width indentation is shown in Fig. 4. Fig. 4(a) and (b) illustrates the x- and y-component values, respectively, of the stabilized external forces at the gray pixels. Fig. 4(c) shows the base-10 logarithms of the ratios of the x-component magnitudes to the y-component magnitudes.

Three fundamental properties can be observed. First, the x-component values are zero at the pixels of the middle column. Second, the component magnitudes of the stabilized external forces are symmetric. Third, the farther the gray pixel is from the diffusion sources, the smaller the component magnitude is at the pixel. These three properties are independent of W and L, but are determined by the iterative solution (20) and the diffusion sources (i.e., initial external forces at the indentation boundary).

According to the first and third properties, we can reasonably conjecture that when the gradient vectors at the LTI boundaries are well preserved, the force components pointing toward the LTI bottom are smaller (or even much smaller) in magnitude than their orthogonal counterparts at the central part of each column (except the middle one) due to the smaller number of diffusion sources and the larger diffusion distances. To verify this conjecture, we can look into the relationship between the x-component magnitudes and the y-component magnitudes at the gray pixels when the 81 × 81-pixel indentation is gradually changed to a long and thin one by keeping L fixed and decreasing W (from 81 to 5).

Following the third property, from Fig. 4 we can see that for the gray pixels in each row, the x-component magnitude decreases from the end pixel to the center pixel, and is minimum (equal to 0) at the center pixel. In contrast, the y-component magnitude increases from the end pixel to the center pixel, and is maximum at the center pixel. Therefore, as shown in Fig. 4(c), the base-10 logarithm of the ratio of the x-component magnitude to the y-component magnitude decreases from the end pixel to the center pixel, and is minimum (negative infinity) at the center pixel. Except the middle column, i.e., $(W+1)/2$th column, the logarithm in each row is minimum in the $(W-1)/2$th and $(W+3)/2$th columns. Therefore, according to the second property, we only need to examine the logarithms of the ratios in the $(W-1)/2$th column to verify our conjecture.

Fig. 5 shows such logarithms and the corresponding x- and y-component values with a fixed L (81) and decreasing W (from 81 to 5). From Fig. 5(a) and (b) we can see that the x- and y-component magnitudes increase and decrease, respectively, as W decreases. Therefore, as demonstrated in Fig. 5(c), the base-10 logarithms of the ratios increase as W decreases from 81 to 5. When the indentation becomes long and thin, the x-component magnitudes are significantly greater than the y-component magnitudes at the pixels near the center.

Similar to Fig. 5, Fig. 6 explores the stabilized external forces at the gray pixels of the middle column with a fixed length L (81) and decreasing odd-width W (from 81 to 3). As described above, the x-component values are zero. As shown in Fig. 6(a), though the y-component magnitudes are maximum at the pixels of the middle column, some of them are close to zero at the pixels near the center when the

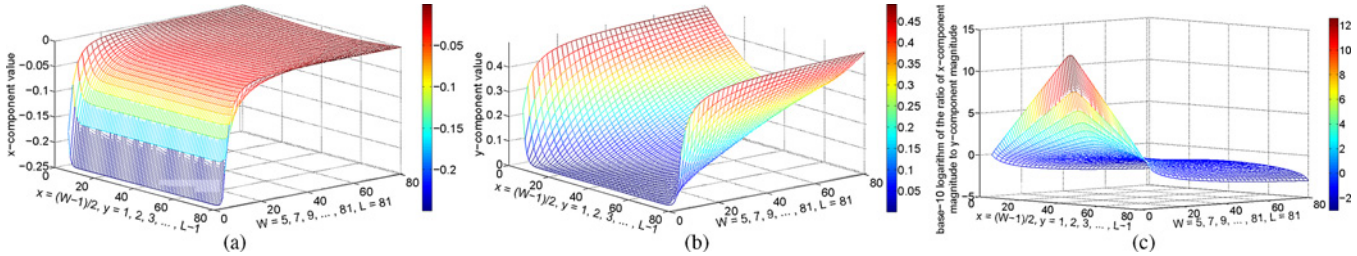

Fig. 5. (a) x- and (b) y-component values of the stabilized external forces at the gray pixels of the $(W-1)/2$th column. (c) Base-10 logarithms of the ratios of the corresponding x-component magnitudes to the y-component magnitudes.

indentation becomes long and thin. The base-10 logarithms of these magnitudes are shown in Fig. 6(b).

After the investigation of the stabilized external forces, we further explore their characteristics during their iterative process. As shown in Fig. 3, the magnitudes of the initial external forces at the gray pixels are zero. As the iteration proceeds, the diffusion sources are diffused farther away from the boundary and into the gray pixel region. The x-components of the diffusion sources will be diffused over the entire gray pixel region earlier than the y-components due to the smaller diffusion distances. And then the y-components will be diffused to every gray pixel. As the iteration continues, the magnitude of each external force component at each gray pixel increases until the iteration converges.

When the x-components of the diffusion sources are diffused over the entire gray pixel region for the first time, the x-component magnitude in the gray pixel region is minimum at the pixels of the $(W-1)/2$th and $(W+3)/2$th columns (except the middle one). From (20) we can obtain that the minimum magnitude is equal to $(1/4)^{(W-1)/2}$. From Fig. 6(b) we can see that even the minimum magnitude is significantly greater than the y-component magnitudes of the stabilized vectors at the pixels of the central part of the middle column. Hence, it is concluded that after the diffusion sources are diffused over the gray pixel region, the x-component magnitudes are always significantly greater than the y-component magnitudes at the pixels of the central part of each column (except the middle one) whenever the iteration terminates. Similarly, we can also obtain the same force characteristic of GGVF in every column within the even-width LTI, as well as the GVF force characteristic for both odd- and even-width LTIs.

IV. Two Problems in GGVF Convergence to LTIs

Resulting from the force characteristic described above, two intrinsic difficulties are identified for the GGVF convergence to LTIs in this section. The first difficulty, referred to as the obliteration problem, is that the significantly smaller force components pointing toward the LTI bottom are obliterated by their orthogonal counterparts at the normalization step. We note that this problem can be coincidentally avoided when the LTI width is an odd number of pixels. The second difficulty, termed the noise problem, comes from noise which can easily affect these smaller force components during the iterative process. Both problems lead to poor convergence to LTIs.

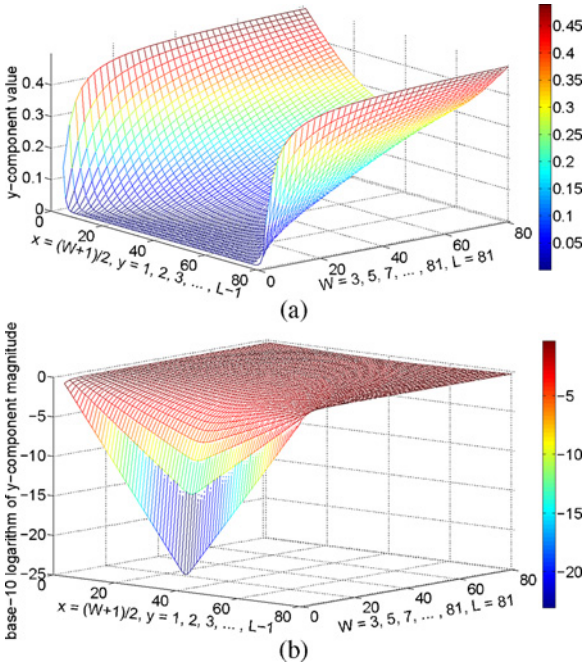

Fig. 6. (a) y-component values of the stabilized vectors at the gray pixels of the middle column. (b) Base-10 logarithms of the y-component magnitudes.

A. Obliteration Problem in GGVF

Due to the force characteristic within the odd-width LTI, in the normalization process (16), the force components pointing toward the LTI bottom are obliterated by their orthogonal counterparts at the pixels of the central part of each column, except the middle one where the obliteration can coincidentally be avoided owing to the zero x-component magnitudes. The desired consistently downward forces of magnitude 1 are thus obtained in the middle column, which can drive the snake into the LTI bottom as shown in Fig. 1(c) and (d). Unlike the odd-width LTI, the even-width LTI has no such middle column, as shown in Fig. 2. With the normalization, the y-components are obliterated by their orthogonal counterparts at the pixels of the central part of each column. As a result, although the consistently downward components do exist, they are too weak to be observed, as shown in Fig. 2(d). During the contour convergence process, these components may have no effect on pulling the snake toward the LTI bottom, and are readily overwhelmed by the internal forces, leading to a wrong convergence result, as shown in Fig. 2(c).

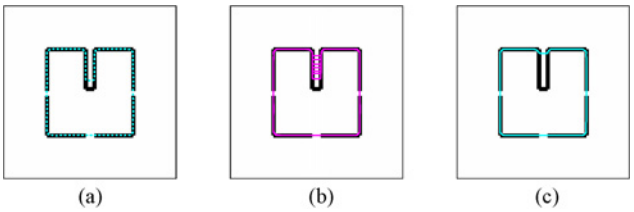

Fig. 7. GGVF snake convergence to an even-width LTI. (a) Initial snake (cyan dashed line). (b) Evolving contours (magenta solid lines). (c) Resulting GGVF snake (cyan solid line).

To verify the above claims, Fig. 7 shows a new GGVF convergence to the even-width LTI by replacing the initialization in Fig. 2(c) with a new one in Fig. 7(a). Fig. 7(b) displays a sequence of curves marked by magenta solid lines depicting the iterative progression of the GGVF snake. Fig. 7(c) shows the stabilized GGVF snake represented by a cyan solid line, which is almost the same as that in Fig. 2(c). As shown in Fig. 7, although the consistently downward components do exist, they are too weak to prevail over the internal forces, which are designed to shrink and smooth the active contour.

B. Noise Problem in GGVF

It was reported in [26] that GGVF snakes outperform GVF snakes in the convergence to LTIs. GVF's difficulty of forcing a snake into an LTI is caused by the over-smoothing of the field near the LTI boundary, governed by the smoothing coefficient μ in (9). When a much smaller μ is used, the GVF snake can also achieve a good convergence to the LTI. However, a satisfactory explanation for their observations was not provided in [26]. This subsection points out that since the force components pointing toward the LTI bottom are significantly smaller in magnitude than their orthogonal counterparts at some pixels, these components are easily affected by noise. In addition, the larger the tradeoff parameter k, the greater the impact of noise. Therefore, it is necessary to estimate the appropriate maximum k for a given $W \times L$-pixel indentation.

1) *Noise Effect on GGVF External Forces:* As described in Section III-A, by choosing a small enough $k > 0$, the iterative solution of the GGVF external forces at the indentation boundary can be approximately written as (18). As a result, the edge map gradients at the indentation boundary are always well preserved, which act as shields impenetrable to the diffusing external forces. Meanwhile, the diffusion sources of the GGVF external forces within the LTI are found to be mainly the edge map gradients at the black indentation boundary.

According to (11) and (12), we can see that as k increases, $g(|\nabla f|)$ and $h(|\nabla f|)$ in (15) increases and decreases, respectively. That means, as k becomes larger, the GGVF external forces at the indentation boundary are more easily changed and their shielding effects decrease in the iterative process. As a result, besides the edge map gradients at the LTI boundary, the diffusion sources of the GGVF external forces within the LTI also contain the remaining edge map gradients within the image, which can be viewed as noise in generating the desired consistently downward components.

As analyzed in Section III, the horizontal components derived from the edge map gradients at both side edges are substantially larger in magnitude than the downward components derived from the edge map gradients at the bottom. Consequently, the vertical noises from both side edges can easily affect the consistently downward components, which are critical for moving the snake into the LTI bottom.

2) *Relationship between k and Noise:* According to (15) and (20), we can find that the vertical noises become larger with an increasing k. That means, the directional consistency of the resulting aggregated components, i.e., the combination of the consistently downward components and the components generated from the vertical noises, is more likely to be disrupted as k increases. When the GGVF external force reaches a stable value, i.e., $\mathbf{v}(x, y, t + \Delta t) = \mathbf{v}(x, y, t)$, the theoretical maximum noise occurs [26]. Substituting the equation into the iterative solution (15) yields the following

$$\frac{1}{4}g(|\nabla f|)\mathbf{A} * u(x, y, t) - \frac{1}{4}h(|\nabla f|)[u(x, y, t) - f_x(x, y)] = 0 \tag{23a}$$

$$\frac{1}{4}g(|\nabla f|)\mathbf{A} * v(x, y, t) - \frac{1}{4}h(|\nabla f|)[v(x, y, t) - f_y(x, y)] = 0. \tag{23b}$$

As shown in Fig. 3, for each black pixel at both side edges of the indentation, we can get $\nabla f = (0.5, 0)$ or $\nabla f = (-0.5, 0)$, and then $|\nabla f| = 0.5$. Because the initial y-component value is equal to 0, the vertical noise is the stabilized y-component value $v(x, y, t)$, corresponding to $v^n_{x,y}$. By substituting $f_y(x, y) = 0$ and $|\nabla f| = 0.5$ into (23a), we can obtain the maximum $|v^n_{x,y}|$, i.e., the magnitude of the maximum vertical noise, as follows:

$$\begin{aligned} \left|v^n_{x,y}\right| &= \left|\frac{g(|0.5|)}{4g(|0.5|)+h(|0.5|)}\left(v^n_{x-1,y}+v^n_{x,y+1}+v^n_{x+1,y}+v^n_{x,y-1}\right)\right| \\ &= \frac{g(|0.5|)}{3g(|0.5|)+1}\left|v^n_{x-1,y}+v^n_{x,y+1}+v^n_{x+1,y}+v^n_{x,y-1}\right| \\ &< g(|0.5|)\left(\left|v^n_{x-1,y}\right|+\left|v^n_{x,y+1}\right|+\left|v^n_{x+1,y}\right|+\left|v^n_{x,y-1}\right|\right) \\ &\le 2g(|0.5|) \\ &= 2\exp(-1/2k) \end{aligned} \tag{24}$$

which is determined by k and increases as k increases. Similarly, the external force components generated from these maximum vertical noises at both side edges of the indentation can also be calculated by solving a system of $(W-2)\times(L-1)$ linear equations. By ensuring that these component magnitudes are less than the corresponding downward component magnitudes, we can obtain the appropriate maximum k, which is determined by W and L as well as the initial external forces at the indentation boundary.

When a larger k is selected, the consistently downward components are very likely to be destroyed. As shown in Fig. 1(h), the over-smoothed GGVF field has no such components, but some upward components within the odd-width LTI. As a result, the snake using the over-smoothed GGVF field is unable to protrude into the LTI, as shown in Fig. 1(g). Similarly, the over-smoothed GGVF field also has no such components within the even-width LTI in Fig. 2(h). But since the internal forces are dominant within the even-width LTI, the vertical components almost have no effect on the convergence result, as shown in Fig. 2(c) and (g).

Similarly, we can also obtain that GVF has the same two difficulties as GGVF in generating the desired external forces for moving the snake into LTIs. Note that since GVF and GGVF show the same speed for diffusing external forces, the same number of iterations is required for achieving the desired GVF and GGVF fields, which, in turn, verifies our new observations in Figs. 1 and 2 that the two snakes exhibit almost the same performance in terms of convergence to LTIs.

V. Proposed CN-GGVF Snake Model

The solutions to the above two intrinsic problems are highly desirable for GVF and GGVF snakes. The noise problem can be solved by appropriately selecting the smoothness degree of the vector fields. In this section, we focus on the obliteration problem by developing an improved external force.

A. Component-Normalized GGVF Field

As described above, the obliteration problem occurs when (16) is employed to normalize an external force vector with two components having a significant difference in magnitude. To solve this problem, the smaller component should be increased so that each component can affect the snake deformation. It is straightforward to see that by separately normalizing each component of the initial GGVF vector with respect to its own magnitude, each normalized component takes the same effect on driving snakes. The new generated external force, which we refer to as component-normalized GGVF (CN-GGVF) field $\mathbf{v}_{\mathrm{cn-ggvf}}(x, y) = [u_{\mathrm{cn-ggvf}}(x, y), v_{\mathrm{cn-ggvf}}(x, y)]$, is thus defined as

$$u_{\mathrm{cn-ggvf}}(x, y) = \begin{cases} 1, & u(x, y) > 0 \\ 0, & u(x, y) = 0 \\ -1, & u(x, y) < 0 \end{cases} \tag{25}$$

$$v_{\mathrm{cn-ggvf}}(x, y) = \begin{cases} 1, & v(x, y) > 0 \\ 0, & v(x, y) = 0 \\ -1, & v(x, y) < 0 \end{cases} \tag{26}$$

where $u(x, y)$ and $v(x, y)$ are the x- and y-components, respectively, of the external force at (x, y) in the GGVF field. Equations (25) and (26) are the sign function. Therefore, the CN-GGVF field is simply rewritten as

$$\mathbf{v}_{\mathrm{cn-ggvf}}(x, y) = \left[\mathrm{sgn}\left(u(x, y)\right), \mathrm{sgn}\left(v(x, y)\right)\right] \tag{27}$$

where $\mathrm{sgn}(\cdot)$ denotes the sign function. Equation (27) is essentially a vector normalization approach. Different from (16) that is termed as vector-based normalization, (27) is referred to as component-based normalization. As in [26], the numerical implementation of (10) specifying the GGVF field[3] can employ either an explicit finite difference method with a stable condition or an implicit scheme that is unconditionally stable.

We call the active contour that uses the CN-GGVF field as its external force a CN-GGVF snake. By replacing the standard external force $F_{\mathrm{ext}}(\mathbf{c}(s)) = -\nabla E_{\mathrm{ext}}(\mathbf{c}(s))$ in (8) with a CN-GGVF field $\mathbf{v}_{\mathrm{cn-ggvf}}(x, y)$, we can obtain the corresponding dynamic CN-GGVF snake equation as

$$\mathbf{c}_t(s, t) = \alpha\mathbf{c}''(s, t) - \beta\mathbf{c}''''(s, t) + \mathbf{v}_{\mathrm{cn-ggvf}}(\mathbf{c}(s, t)) \tag{28}$$

which can be solved numerically using the finite difference approach of the traditional snake given in Section II-A.

[3]In this paper, (10) is replaced by $\mathbf{v}_t(x, y, t) = g(|\nabla f|)\times\left[g(|\nabla f|)\mathbf{v}_{\mathrm{NN}}(x, y, t) + h(|\nabla f|)\mathbf{v}_{\mathrm{TT}}(x, y, t)\right] - h(|\nabla f|)\left[\mathbf{v}(x, y, t) - \nabla f\right]$ to calculate the GGVF field [27], [34], such that a larger range is available for k to avoid the noise problem described in Section IV-B.

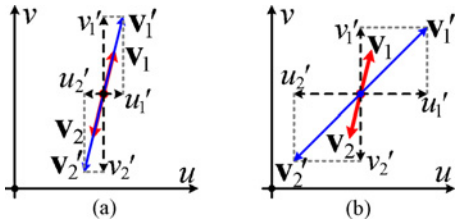

Fig. 8. Effects of (a) vector- and (b) component-based normalization schemes on a pair of initial vectors $\mathbf{v}_1$ and $\mathbf{v}_2$ indicated by red arrows. The normalized vectors $\mathbf{v}_1'$ and $\mathbf{v}_2'$ are marked by blue arrows.

B. Comparisons Between Component- and Vector-Based Normalizations

First, we compare the computational complexity of the component-based normalization with that of the vector-based normalization. To normalize an initial GGVF field derived from an $N \times N$-pixel image, the vector-based normalization requires $2 \times N \times N$ multiplication operations, $2 \times N \times N$ division operations, and $N \times N$ square root operations. While the proposed normalization only needs $2 \times N \times N$ comparison operations, comparing favorably to the computational complexity of the original one. Note that the magnitudes of the normalized GGVF vectors calculated by (16) are usually equal to 1, while those of the CN-GGVF vectors are $\sqrt{2}$ generally.

Then we compare the effects of the two normalization methods on a pair of initial GGVF vectors at the object boundary. As illustrated in Fig. 8, the initial vectors $\mathbf{v}_1$ and $\mathbf{v}_2$ indicated by red arrows are equal in magnitude and opposite in direction, and the normalized vectors $\mathbf{v}_1'$ and $\mathbf{v}_2'$ are marked by blue arrows. Fig. 8(a) shows the normalized GGVF vectors computed using the vector-based normalization (16). Compared with the initial ones, the magnitudes of the normalized vectors are altered, while their orientations are preserved. Fig. 8(b) shows the CN-GGVF external forces calculated using the proposed component-based normalization (27), causing changes in both magnitude and orientation. While it should be noted that the pair of the CN-GGVF vectors are still equal in magnitude and opposite in direction. In comparison, the effect of the proposed normalization on the directional change can be viewed as a reduction in the directional resolution.

C. Comparisons Between CN-GGVF and GGVF Convergence Behaviors

As mentioned above, the edge map gradient used as an external force for the traditional snake can only drive the snake to the object edges in the vicinity of the edges. GGVF is to extend the effect of the edge map gradient farther away from the edges, and is thus defined as a diffusion of the gradient vectors of an edge map [26]. The resulting field will

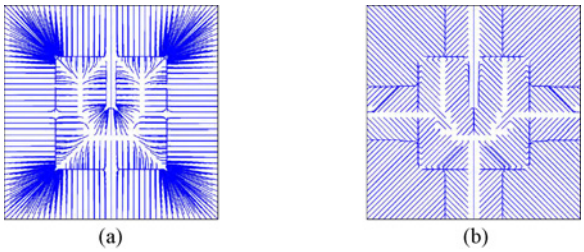

Fig. 9. Streamlines of particles placed in (a) GGVF field and (b) CN-GGVF field.

conform to the edge map gradient at strong edges, but will vary smoothly away from the boundaries. And the resulting GGVF external forces will point to and move the snake toward the strong boundaries (mostly the desired boundaries). Under the influence of the internal forces and the GGVF field, the snake will deform and finally stop moving at the desired boundaries, where the external force at each snaxel (snake elements) points to the opposite direction of the movement.

As described above, compared with the normalized GGVF field, the CN-GGVF field changes not only the magnitudes but also the directions of the initial vectors. From (28) we can see that the magnitude changes will lead to the alteration in the convergence speed of the snake, while the direction changes will alter the convergence trajectory and may alter the convergence result. Since the effect of the proposed normalization on the vector directions is only to reduce the directional resolution, the CN-GGVF field is still relatively smooth. As a result, the CN-GGVF external forces can also move the snake toward the desired boundaries. On the other hand, since the CN-GGVF external forces at the desired boundaries are still equal in magnitude and opposite in direction, the snake will still stop at the desired boundaries. Hence, it is concluded that if the effect of the internal forces is not taken into account (only the effect of the external forces is discussed here), the CN-GGVF snake will converge to the same result as that of the GGVF snake under the same initial conditions, although with different paths and speeds.

D. Streamlines

Streamlines are the paths where free particles move when placed in a vector field [15]. The capture ranges and motion inducing properties of various external forces can be observed by looking at their streamlines. Fig. 9(a) and (b) shows the streamlines of particles placed in a GGVF field and a CN-GGVF field, respectively, to further compare the convergence behaviors of the two snakes. Both the vector fields are derived from an edge map of the above line-drawing with an odd-width LTI in Fig. 1. From Fig. 9 we can see that the particle trajectories driven by the CN-GGVF field are different from those driven by the GGVF field, while that the free particles are drawn toward and eventually stopped at the object boundaries in Fig. 9(b) is exactly the same as that in Fig. 9(a). As none of these free particles deforms under the internal force, Fig. 9 confirms that without considering the effect of the internal forces, the proposed CN-GGVF snake and the GGVF snake will converge to the same result under the same initial conditions, in spite of deforming along different paths and at different speeds.

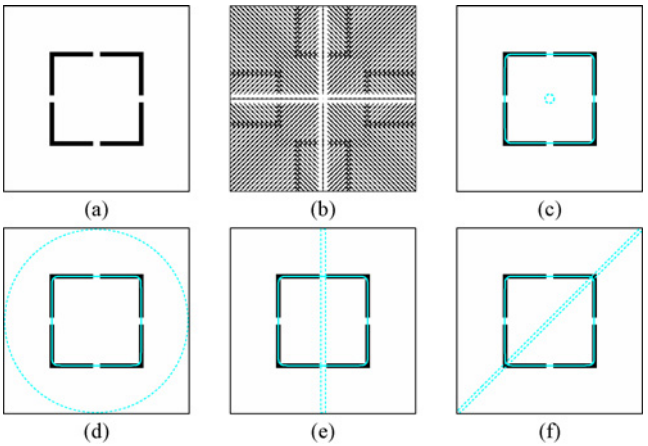

Fig. 10. (a) 81×81-pixel line-drawing of a square with broken boundaries. (b) CN-GGVF field. (c)–(f) Resulting CN-GGVF snakes (cyan solid lines) from four different initializations (cyan dashed lines).

VI. Experimental Results and Analysis

This section demonstrates several desirable properties of CN-GGVF snakes. To exemplify the advantages of the proposed snakes over GGVF snakes, we compare the qualitative performance of the two snakes on both synthetic and real images. We employ $\alpha = 1$ and $\beta = 0$ for all snakes, which are dynamically reparameterized during deformation to maintain contour point separation to within 0.5–1.5 pixels [35]. For each test image, the same initial contour (indicated by a dashed line) and parameter values are used for both the snakes (indicated by solid lines). All edge maps used in active contours are normalized to the range [0, 1].

A. Capture Range and Initialization Sensitivity

We use a square-shaped line-drawing to evaluate the performance of the CN-GGVF snake in terms of capture range and initialization sensitivity. Fig. 10(a) reveals the original 81×81-pixel image with broken boundaries. Fig. 10(b) displays the CN-GGVF field ($k = 0.01$ and $n = 81$) derived from an edge map computed using $-I(x, y)$. Fig. 10(c)–(f) shows a set of stabilized CN-GGVF snakes from four different initializations. Using the vector field in Fig. 10(b) as an external force, the CN-GGVF active contour can converge correctly from these four initializations placed inside, outside, and across the desired boundary. In addition, as the initializations in Fig. 10(c) and (d) are far away from the square-shaped object, the CN-GGVF snake appears to have both an insensitivity to initialization and a large capture range.

B. Convergence to LTIs

Fig. 11 compares the performance of the CN-GGVF snake in capturing LTIs with that of the GGVF snake. We use four 160×160-pixel square-shaped line-drawings with 5-, 6-, 7-, and 8-pixel-width LTIs as test images. In Fig. 11, all edge maps are computed using $-I(x, y)$. $k = 0.01$ is selected to calculate the appropriately smoothed GGVF and CN-GGVF

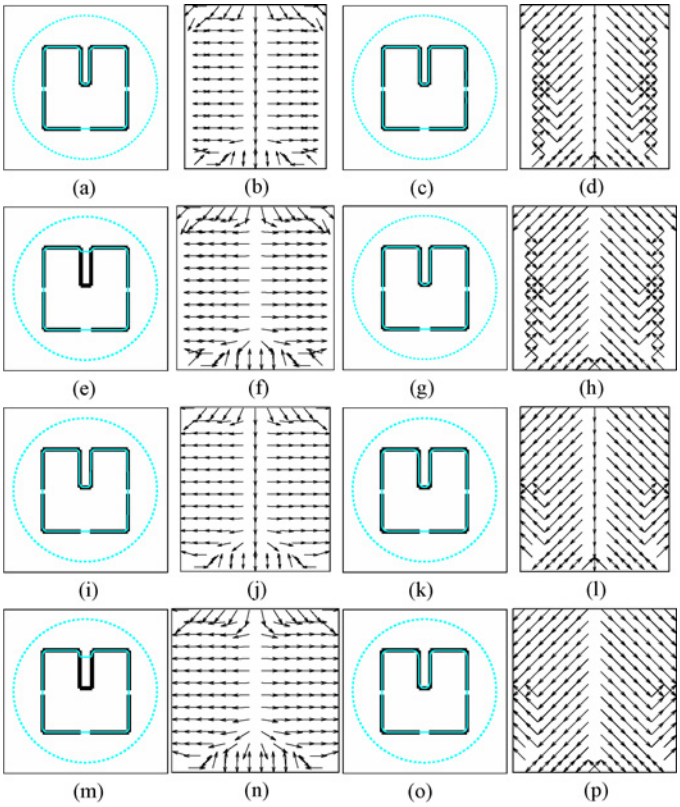

Fig. 11. Performance of GGVF and CN-GGVF snakes in capturing LTIs. The original images are 160 × 160-pixel line-drawings with 5-, 6-, 7-, and 8-pixel-width LTIs in the first, second, third, and fourth rows, respectively. First column: GGVF snakes. Second column: GGVF external forces within LTIs. Third column: CN-GGVF snakes. Fourth column: CN-GGVF external forces within LTIs. (a) GGVF snake. (b) 5-pixel-width. (c) CN-GGVF snake. (d) 5-pixel-width. (e) GGVF snake. (f) 6-pixel-width. (g) CN-GGVF snake. (h) 6-pixel-width. (i) GGVF snake. (j) 7-pixel-width. (k) CN-GGVF snake. (l) 7-pixel-width. (m) GGVF snake. (n) 8-pixel-width. (o) CN-GGVF snake. (p) 8-pixel-width.

fields with $n = 160$. All fields within the LTIs are displayed, which are sampled by a factor of 3 in the vertical direction. All resulting snakes are derived from a same initialization. We compare the two snakes in terms of the external forces as well as the convergence results and speeds of the contours as follows.

1) *External Forces Within LTIs:* As analyzed in Section III, when the GGVF field is appropriately smoothed, the downward force components are generated at every pixel within all LTIs. After the vector-based normalization, the consistently downward forces of magnitude 1 are obtained at the pixels of the middle column where the x-component magnitudes are 0, as shown in Fig. 11(b) and (j). And some components are obliterated by their orthogonal counterparts because of their substantially smaller magnitudes, as shown in Fig. 11(b), (f), (j), and (n). As we can see in Fig. 11(d), (h), (l), and (p), when the initial GGVF vectors are normalized by the proposed component-based scheme, the consistently downward and significant components are obtained at every pixel within all LTIs, which confirms our analysis that the downward components are presented at all pixels within the LTIs, and some components are considerably smaller in magnitude than their orthogonal counterparts.

2) *Convergence Results of Snakes:* Because of the presence of the consistently downward and significant components in Fig. 11(b) and (j), the GGVF snakes in Fig. 11(a) and (i) are able to converge completely to the odd-width LTIs. In contrast, since there are no such components in Fig. 11(f) and (n), the GGVF snakes in Fig. 11(e) and (m) fail to capture the even-width LTIs. Compared with the GGVF snakes, the CN-GGVF snakes successfully eliminate the obliteration problem, and are therefore capable of detecting all LTIs, as shown in Fig. 11(c), (g), (k), and (o). We note that the GGVF snake result in Fig. 11(m) is slightly better than that in Fig. 11(e), which can be attributed to both the increasing number of the downward components within the wider LTI and the increasing magnitudes of these components, as analyzed in Section III. As the even-width LTI becomes wider, the GGVF snake becomes more likely to detect it.

3) *Convergence Speeds of Snakes:* After external forces are obtained, snakes will deform under the influence of internal and external forces to conform to the desired boundaries until they converge. The GGVF snakes in Fig. 11(a), (e), (i), and (m) converge after 680, 80, 420, and 240 iterations, respectively, and the CN-GGVF snakes in Fig. 11(c), (g), (k), and (o) converge after 128, 100, 88, and 80 iterations, respectively. We can see that as the LTI becomes wider, the iteration number required for the stabilized CN-GGVF snake decreases. Similarly, the iteration number required for the GGVF snake convergence to an odd-width LTI decreases. Compared with the GGVF snake convergence, the corresponding CN-GGVF snake convergence requires a much smaller number of iterations owing to the proposed component-based normalization. Since the two snakes differ greatly in the reconstruction of the even-width LTI, it makes no sense to compare the iteration number between them.

As shown in Fig. 11, the CN-GGVF snake significantly improves the performance of the GGVF snake in capturing the LTIs. Specifically, the CN-GGVF snake achieves remarkably faster convergence speed in capturing the odd-width LTIs. Furthermore, since the proposed normalization eliminates the obliteration problem that plagues the GGVF snake, the CN-GGVF snake is thus able to detect the even-width LTIs, while also obtaining fast convergence speed. To further demonstrate its superior performance in terms of capturing the LTIs with different widths, the CN-GGVF snake is compared with various state-of-the-art snakes, as shown in Fig. 12. Corresponding to Fig. 12, Table I gives some statistics on the iteration numbers of various snakes. It is straightforward to find that the proposed CN-GGVF snake is the most efficient one.

C. Noise Sensitivity

Snakes can sometimes be very sensitive to noise. The GGVF and CN-GGVF snakes are applied to an impulse noise corrupted U-shaped image to evaluate their noise sensitivity. The noisy 64×64-pixel image is illustrated in Fig. 13(a). Fig. 13(b) shows an edge map computed using $G_\sigma(x, y) * I(x, y)$, where the Gaussian filter $G_\sigma(x, y)$ with $\sigma = 1$ is applied to suppress the noise. In addition, appropriate α, β, k, and n should be selected to ensure the internal forces or the accumulated forces

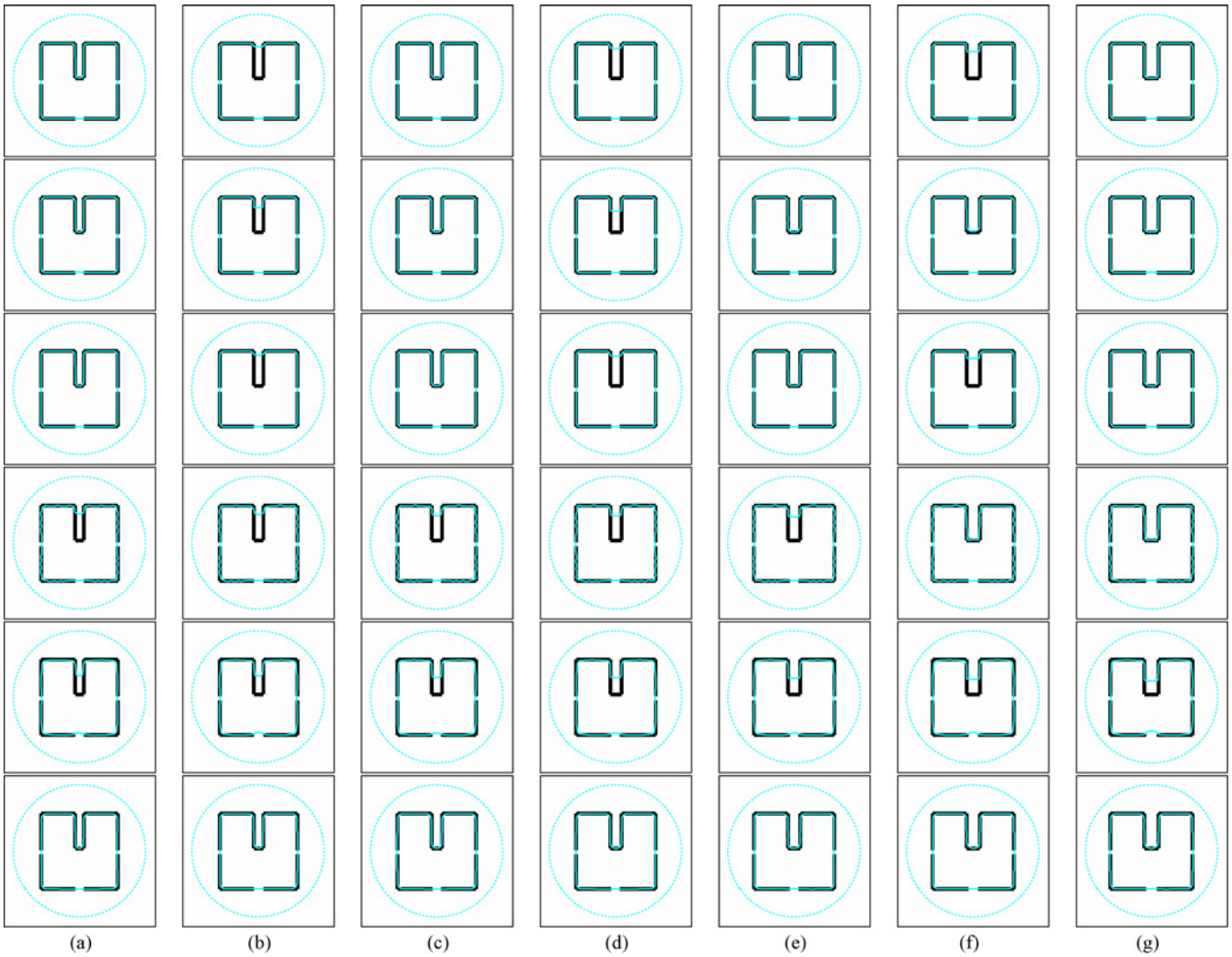

Fig. 12. Performance of GGVF, NGVF, NBGVF, DDGVF, VFC, and CN-GGVF snakes in capturing LTIs. The original images are 160 × 160-pixel line-drawings with 5-, 6-, 7-, 8-, 9-, 10-, and 11-pixel-width LTIs in columns (a), (b), (c), (d), (e), (f), and (g), respectively. First row: GGVF snakes. Second row: NGVF snakes. Third row: NBGVF snakes. Fourth row: DDGVF snakes. Fifth row: VFC snakes. Sixth row: CN-GGVF snakes.

TABLE I
ITERATION NUMBER FOR CONTOUR CONVERGENCE TO LTIS, CORRESPONDING TO FIG. 12

	5-pixel	**6-pixel**	**7-pixel**	**8-pixel**	**9-pixel**	**10-pixel**	**11-pixel**
GGVF	680	–	420	–	300	–	220
NGVF	260	–	200	–	160	180	148
NBGVF	620	–	440	–	280	–	244
DDGVF	–	–	–	–	–	152	120
VFC	–	–	–	–	–	–	–
CN-GGVF	128	100	88	80	76	72	72

The symbol "–" denotes that the corresponding snake cannot converge to the LTI bottom.

of the desired boundary are able to overwhelm the forces generated from the noise. Generally, these parameters should be increased as the noise level increases. In this experiment, $k = 3$ and $n = 128$ are selected to calculate the two vector fields. As a result, both the GGVF and CN-GGVF snakes converge well to the dominant U-shaped boundary, as shown in Fig. 13(c) and (d), respectively. The two results, barely distinguishable from each other, demonstrate the superior noise robustness of the two snakes. Fig. 14 further demonstrates that the CN-GGVF snake is less sensitive to Gaussian noise than other snakes when capturing the LTIs. In the following experiments, the noise sensitivity of the proposed snake will be examined by applying it to some real images.

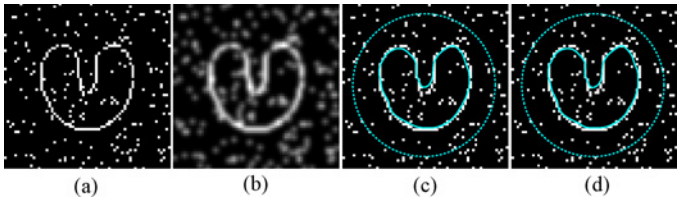

Fig. 13. (a) Noisy U-shaped image. (b) Edge map $G_\sigma(x, y) * I(x, y)$ with $\sigma = 1$. Results (cyan solid lines) of (c) GGVF and (d) CN-GGVF snakes ($k = 3$ and $n = 128$) from a same initialization (cyan dashed line).

D. Real Images

1) *Photographic Image:* Experiments are performed on real-photographic images to demonstrate the superior perfor-

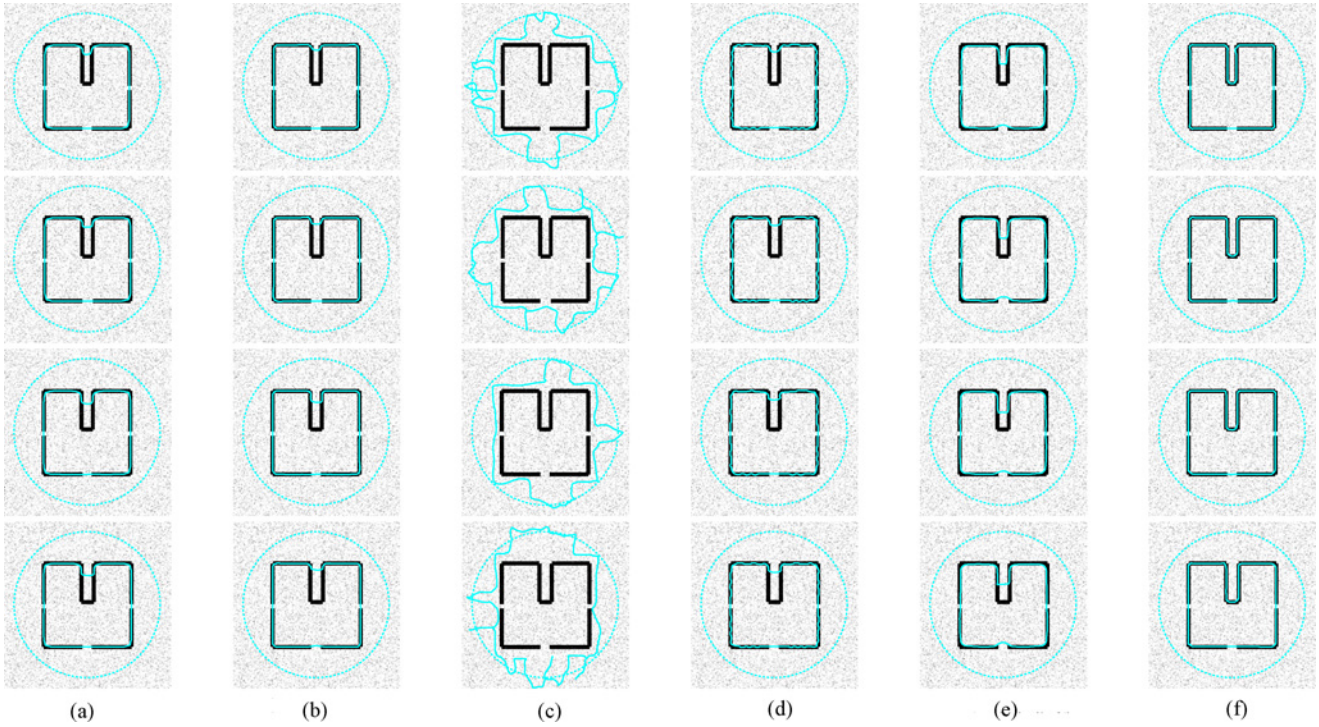

Fig. 14. Performance of GGVF, NGVF, NBGVF, DDGVF, VFC, and CN-GGVF snakes in capturing LTIs with Gaussian noise. The original images are 160 × 160-pixel line-drawings with 5-, 6-, 7-, and 8-pixel-width LTIs in the first, second, third, and fourth rows, respectively. (a) GGVF snakes. (b) NGVF snakes. (c) NBGVF snakes. (d) DDGVF snakes. (e) VFC snakes. (f) CN-GGVF snakes.

mance of the CN-GGVF snake over the GGVF snake in terms of capturing object boundaries, in particular the LTI boundaries. As shown in Fig. 15, five images are used to evaluate the performance. For the first one in Fig. 15(a), the goal is to segment the *Rocket*. Fig. 15(b) shows an edge map $|\nabla[G_\sigma(x, y) * I(x, y)]|^2$ with $\sigma = 0.5$, which is used to calculate both the fields with $k = 0.1$ and $n = 200$. As shown in Fig. 15(c), the GGVF snake fails to converge to both ends of the *Rocket*, which represent LTIs when viewed from the inside of the *Rocket*. The main reason for the failure is that the external force components pulling the snake to both ends of the *Rocket* are smaller in magnitude than the internal forces which shrink the contour. After these components are increased by the proposed component-based normalization, they are able to move the CN-GGVF snake into both ends of the *Rocket*, as shown in Fig. 15(d). For the second image, the desired boundary is the outline of the *Fighter aircraft*. Fig. 15(f) shows an edge map $|\nabla[G_\sigma(x, y) * I(x, y)]|^2$ with $\sigma = 0.5$. Since the *Fighter aircraft* is relatively small in the image, $n = 100$ iterations are performed to calculate both the fields with $k = 0.1$. For the same reason as above, the GGVF snake in Fig. 15(g) fails to capture the aircraft nose, while the CN-GGVF snake in Fig. 15(h) reconstructs the aircraft boundary quite well. For the third image, we aim to segment the depth *Vernier caliper*. Compared with the above two images, the third one contains more noise, in particular the depth scales. To suppress the noise, a larger $\sigma = 3$ is selected to compute an edge map $|\nabla[G_\sigma(x, y) * I(x, y)]|^2$, as shown in Fig. 15(j). In addition, a larger $k = 2$ is used to calculate both the vector fields with $n = 400$. As a result, the GGVF snake shown in Fig. 15(k) succeeds in detecting the desired object except the fixed scale at both sides due to the same reason as above. By contrast, the CN-GGVF snake result in Fig. 15(l) shows an excellent convergence to the desired boundary, despite the initialization from far away, the image noise, and the LTIs. For the *Bear* and *Woman face* images in Fig. 15(m) and (q), respectively, it can be seen that better reconstructions are obtained by the CN-GGVF snake than the GGVF snake. Experiments and comparisons against the GGVF snake demonstrate that the proposed CN-GGVF snake yields better performance in capturing object boundaries in real photographic images, and possesses the superior robustness to noise.

2) *Magnetic Resonance Image:* The GGVF and CN-GGVF snakes are applied to a magnetic resonance image to further test their sensitivity to noise. The test image is a 160 × 160-pixel gray-level image of the left ventricle of a human heart, as shown in Fig. 16(a). The goal of this experiment is to extract the endocardium of the left ventricle. $\sigma = 2.5$ is employed to calculate an edge map $|\nabla[G_\sigma(x, y) * I(x, y)]|^2$ in Fig. 16(b) to suppress the noise. The resulting GGVF and CN-GGVF fields with $k = 0.05$ and $n = 160$ are iteratively calculated from the gradient of the edge map. After 50 iterations, both the GGVF snake in Fig. 16(c) and the CN-GGVF snake in Fig. 16(d) converge, and perform well in reconstructing the endocardial border, including the papillary muscle that protrudes into the cavity at about the 1 o'clock position and can be viewed as an indentation but not an LTI. The two results again demonstrate the outstanding noise robustness of both the snakes.

E. Object Tracking

In this section, *human heart* and *goldfish* video sequences are employed to evaluate the tracking performance of the

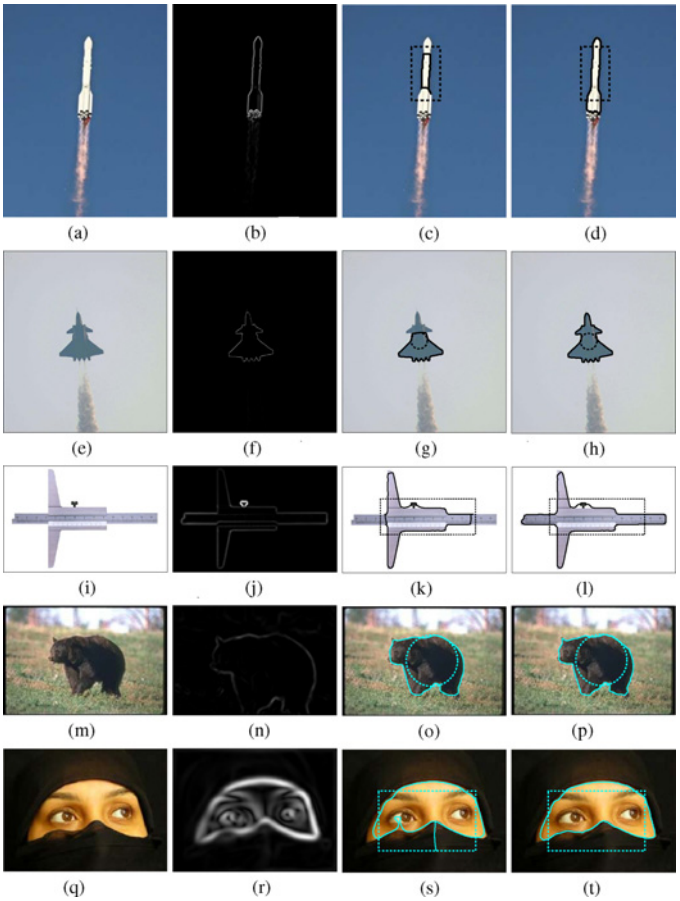

Fig. 15. Performance of GGVF and CN-GGVF snakes on photographic images. (a) *Rocket*. (e) *Fighter aircraft*. (i) *Vernier caliper*. (m) *Bear*. (q) *Woman face*. First column: original images. Second column: edge maps. Third column: GGVF snakes. Fourth column: CN-GGVF snakes. (a) Original image. (b) Edge map. (c) GGVF snake. (d) CN-GGVF snake. (e) Original image. (f) Edge map. (g) GGVF snake. (h) CN-GGVF snake. (i) Original image. (j) Edge map. (k) GGVF snake. (l) CN-GGVF snake. (m) Original image. (n) Edge map. (o) GGVF snake. (p) CN-GGVF snake. (q) Original image. (r) Edge map. (s) GGVF snake. (t) CN-GGVF snake.

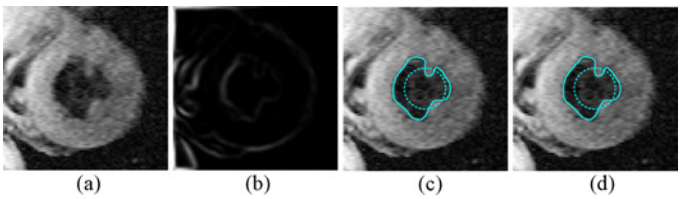

Fig. 16. (a) Magnetic resonance image of the left ventricle of a human heart. (b) Edge map $|\nabla[G_\sigma(x, y) * I(x, y)]|^2$ with $\sigma = 2.5$. Results of (c) GGVF and (d) CN-GGVF snakes from a same initialization.

GGVF and CN-GGVF snakes. Specifically, we initialize the snake in the first frame using a circle around the desired object by hand. For the following frames, however, each snake is automatically initialized by using the resulting contour from the previous frame. The tracking results are shown in Figs. 17 and 18, respectively. It can be seen that under almost the same computational complexity, the CN-GGVF snake outperforms the GGVF snake on both sequences, where more boundary details can be detected by the proposed snake. It is worth noting that the GGVF snake is more sensitive

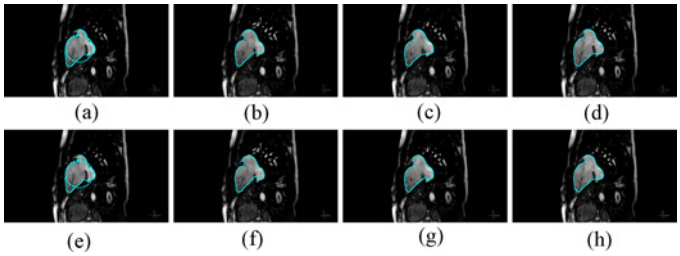

Fig. 17. Performance of GGVF and CN-GGVF snakes in tracking a human heart. First row: GGVF snakes. Second row: CN-GGVF snakes. (a) Frame 1. (b) Frame 6. (c) Frame 14. (d) Frame 20. (e) Frame 1. (f) Frame 6. (g) Frame 14. (h) Frame 20.

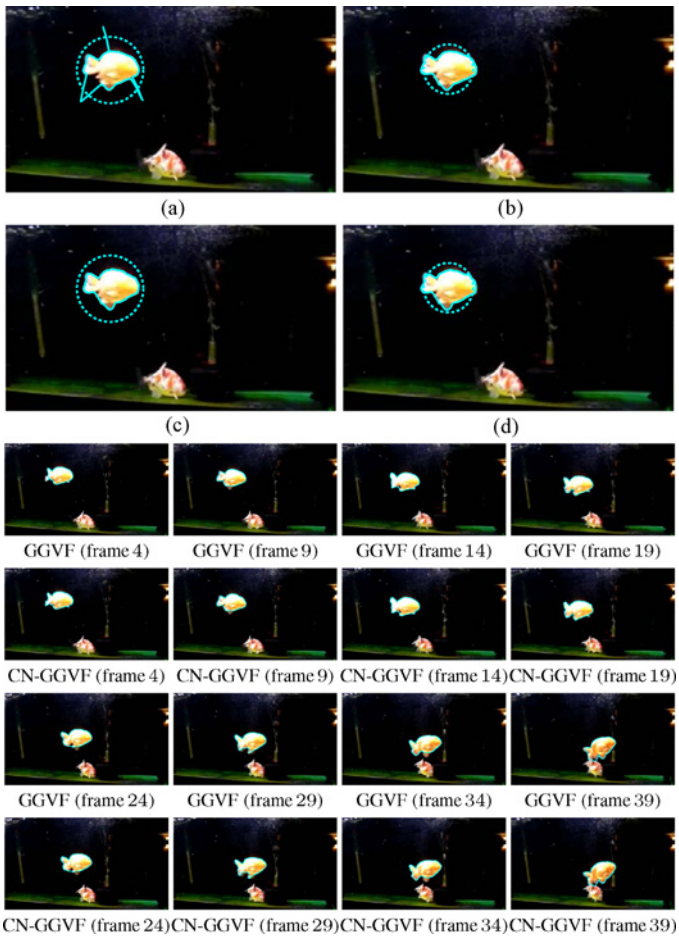

Fig. 18. Performance of GGVF and CN-GGVF snakes in tracking a goldfish. (a) GGVF (frame 1). (b) GGVF (frame 1). (c) CN-GGVF (frame 1). (d) CN-GGVF (frame 1).

to initialization than the CN-GGVF snake, as illustrated in Fig. 18(a) and (c).

VII. Conclusion

In this paper, we argued that at almost the same computational cost, both GVF and GGVF snakes can capture LTIs of odd widths when their vector fields are appropriately smoothed, while the two snakes fail to work when the fields are over-smoothed. On the other hand, both the snakes are generally incapable of converging to even-width LTIs regardless

of the smoothness degree of the fields. We identified the cause behind the convergence problem in GVF/GGVF, that is, the directionally consistent external force components necessary to pull the snake toward the LTI bottoms were significantly smaller in magnitude than their orthogonal counterparts at some pixels which tend to be disturbed during the diffusion or obliterated in the vector-based normalization.

To solve the obliteration problem that plagues GGVF, we proposed component-normalized GGVF (CN-GGVF), which separately normalizes each component of initial GGVF vectors with respect to its own magnitude. Experiments demonstrate that compared with the GGVF snakes, the proposed CN-GGVF snakes were able to capture LTIs regardless of odd or even widths with a faster convergence speed, and achieve lower computational complexity in vector normalization as well as better performance on the real-photographic image testing. Additionally, CN-GGVF preserves other desirable properties of GGVF, such as a wide capture range and robustness to initialization and noise.

REFERENCES

[1] M. Kass, A. Witkin, and D. Terzopoulos, "Snakes: Active contour models," *Int. J. Comput. Vis.*, vol. 1, no. 4, pp. 321–331, 1988.

[2] C. Xu, D. Pham, and J. Prince, "Image segmentation using deformable models," in *Handbook of Medical Imaging. Vol. 2 Medical Image Processing and Analysis*, M. Sonka and J. M. Fitzpatrick, Eds., Bellingham, WA: SPIE, May 2000, ch. 3, pp. 129–174.

[3] X. Xie and M. Mirmehdi, "MAC: Magnetostatic active contour model," *IEEE Trans. Pattern Anal. Mach. Intell.*, vol. 30, no. 4, pp. 632–646, Apr. 2008.

[4] X. Xie, "Active contouring based on gradient vector interaction and constrained level set diffusion," *IEEE Trans. Image Process.*, vol. 19, no. 1, pp. 154–164, Jan. 2010.

[5] N. Paragios and R. Deriche, "Geodesic active contours and level sets for the detection and tracking of moving objects," *IEEE Trans. Pattern Anal. Mach. Intell.*, vol. 22, no. 3, pp. 266–280, Mar. 2000.

[6] N. Ray, S. Acton, and K. Ley, "Tracking leukocytes *in vivo* with shape and size constrained active contours," *IEEE Trans. Medical Imaging*, vol. 21, no. 10, pp. 1222–1235, Oct. 2002.

[7] A. Mansouri, D. Mukherjee, and S. Acton, "Constraining active contour evolution via lie groups of transformation," *IEEE Trans. Image Process.*, vol. 13, no. 6, pp. 853–863, Jun. 2004.

[8] N. Ray and S. Acton, "Motion gradient vector flow: An external force for tracking rolling leukocytes with shape and size constrained active contours," *IEEE Trans. Medical Imaging*, vol. 23, no. 12, pp. 1466–1478, Dec. 2004.

[9] M. Gastaud, M. Barlaud, and G. Aubert, "Combining shape prior and statistical features for active contour segmentation," *IEEE Trans. Circuits Syst. Video Technol.*, vol. 14, no. 5, pp. 726–734, May 2004.

[10] B. Li and S. Acton, "Active contour external force using vector field convolution for image segmentation," *IEEE Trans. Image Process.*, vol. 16, no. 8, pp. 2096–2106, Aug. 2007.

[11] T. Wang, I. Cheng, and A. Basu, "Fluid vector flow and applications in brain tumor segmentatio," *IEEE Trans. Biomed. Eng.*, vol. 56, no. 3, pp. 781–789, Mar. 2009.

[12] P. Ghosh, L. Bertelli, B. Sumengen, and B. Manjunath, "A nonconservative flow field for robust variational image segmentation," *IEEE Trans. Image Process.*, vol. 19, no. 2, pp. 478–490, Feb. 2010.

[13] A. Abrantes and J. Marques, "A class of constrained clustering algorithms for object boundary extraction," *IEEE Trans. Image Process.*, vol. 5, no. 11, pp. 1507–1521, Nov. 1996.

[14] C. Davatzikos and J. Prince, "An active contour model for mapping the cortex," *IEEE Trans. Med. Imag.*, vol. 14, no. 1, pp. 65–80, Mar. 1995.

[15] C. Xu and J. Prince, "Snakes, shapes, and gradient vector flow," *IEEE Trans. Image Process.*, vol. 7, no. 3, pp. 359–369, Mar. 1998.

[16] N. Paragios, "A variational approach for the segmentation of the left ventricle in cardiac image analysis," *Int. J. Comput. Vision*, vol. 50, no. 3, pp. 345–362, Nov. 2002.

[17] N. Paragios, O. Mellina-Gottardo, and V. Ramesh, "Gradient vector flow fast geometric active contours," *IEEE Trans. Pattern Anal. Mach. Intell.*, vol. 26, no. 3, pp. 402–407, Mar. 2004.

[18] J. Cheng and S. Foo, "Dynamic directional gradient vector flow for snakes," *IEEE Trans. Image Process.*, vol. 15, no. 6, pp. 1563–1571, Jun. 2006.

[19] G. Zhu, S. Zhang, Q. Zeng, and C. Wang, "Gradient vector flow active contours with prior directional information," *Pattern Recognit. Lett.*, vol. 31, no. 9, pp. 845–856, Jul. 2010.

[20] Y. Guo and C. Lu, "Multi-modality image registration using mutual information based on gradient vector flow," in *Proc. IEEE Int. Conf. Pattern Recognit.*, vol. 3, Sep. 2006, pp. 697–700.

[21] M. Hassouna and A. Farag, "Variational curve skeletons using gradient vector flow," *IEEE Trans. Pattern Anal. Mach. Intell.*, vol. 31, no. 12, pp. 2257–2274, Dec. 2009.

[22] C. Li, J. Liu, and M. Fox, "Segmentation of external force field for automatic initialization and splitting of snakes," *Pattern Recognit.*, vol. 38, no. 11, pp. 1947–1960, Nov. 2005.

[23] B. Li and S. Acton, "Automatic active model initialization via poisson inverse gradient," *IEEE Trans. Image Process.*, vol. 17, no. 8, pp. 1406–1420, Aug. 2008.

[24] X. Han, C. Xu, and J. Prince, "Fast numerical scheme for gradient vector flow computation using a multigrid method," *IET Image Process.*, vol. 1, no. 1, pp. 48–55, Mar. 2007.

[25] D. Boukerroui, "Efficient numerical schemes for gradient vector flow," *Pattern Recognit.*, vol. 45, no. 1, pp. 626–636, Jan. 2012.

[26] C. Xu and J. Prince, "Generalized gradient vector flow external forces for active contours," *Signal Process.*, vol. 71, no. 2, pp. 131–139, Dec. 1998.

[27] J. Ning, C. Wu, S. Liu, and S. Yang, "NGVF: An improved external force field for active contour model," *Pattern Recognit. Lett.*, vol. 28, no. 1, pp. 58–63, Jan. 2007.

[28] Y. Wang, L. Liu, H. Zhang, Z. Cao, and S. Lu, "Image segmentation using active contours with normally biased GVF external force," *IEEE Signal Process. Lett.*, vol. 17, no. 10, pp. 875–878, Oct. 2010.

[29] J. Cheng, R. Xue, Y. Liu, and W. Lu, "Segmentation of mechanical images using improved active contour model," in *Proc. IEEE Int. Conf. Ind. Technol.*, Apr. 2008, pp. 1–4.

[30] P. Yan and A. Kassim, "Segmentation of volumetric MRA images by using capillary active contour," *Medical Image Anal.*, vol. 10, no. 3, pp. 317–329, Jun. 2006.

[31] J. Mille, R. Bon, and L. Cohen, "Region-based 2D deformable generalized cylinder for narrow structures segmentation," in *Proc. Eur. Conf. Comput. Vision*, Oct. 2008, pp. 392–404.

[32] L. Cohen, "On active contour models and balloons," *CVGIP: Image Understanding*, vol. 53, no. 2, pp. 211–218, Mar. 1991.

[33] L. Cohen and I. Cohen, "Finite-element methods for active contour models and balloons for 2-D and 3-D images," *IEEE Trans. Pattern Anal. Mach. Intell.*, vol. 15, no. 11, pp. 1131–1147, Nov. 1993.

[34] V. Caselles, J.-M. Morel, and C. Sbert, "An axiomatic approach to image interpolation," *IEEE Trans. Image Process.*, vol. 7, no. 3, pp. 376–386, Mar. 1998.

[35] S. Lobregt and M. Viergever, "A discrete dynamic contour model," *IEEE Trans. Medical Imaging*, vol. 14, no. 1, pp. 12–24, Mar. 1995.

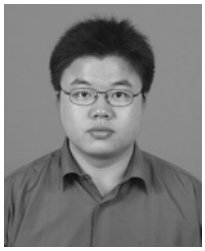

Lunming Qin received the B.E. degree in automation and the M.E. degree in signal and information processing from Beijing Jiaotong University (BJTU), Beijing, China, in 2003 and 2006, respectively. He is currently pursuing the Ph.D. degree in signal and information processing at the Institute of Information Science, BJTU.

His current research interests include image segmentation, object tracking, medical image analysis, deformable models, and computer vision.

Ce Zhu (M'03–SM'04) received the B.S. degree from Sichuan University, Chengdu, China, in 1989, and the M.Eng. and Ph.D. degrees from Southeast University, Nanjing, China, in 1992 and 1994, respectively, all in electronic and information engineering.

He pursued Post-Doctoral Research with the Chinese University of Hong Kong, the City University of Hong Kong, and the University of Melbourne, Melbourne, Australia. He was with the School of Electrical and Electronic Engineering, Nanyang Technological University, Singapore, from 1998 to 2012. He is currently a Professor with the School of Electronic Engineering, University of Electronic Science and Technology of China, Chengdu. He has held visiting positions with Queen Mary, University of London, London, U.K., and Nagoya University, Nagoya, Japan. His current research interests include image/video coding, streaming and processing, 3-D video, joint source-channel coding, multimedia systems, and applications.

Dr. Zhu serves on the editorial boards of six international journals, including as an Associate Editor of the IEEE TRANSACTIONS ON BROADCASTING, the IEEE SIGNAL PROCESSING LETTERS, *Multidimensional Systems*, and *Signal Processing* (Springer), an Area Editor of *Signal Processing: Image Communication* (Elsevier), an editor of IEEE COMMUNICATIONS SURVEYS AND TUTORIALS, and as an Editorial Board Member of *Multimedia Tools and Applications* (Springer). He has served on technical/program committees, organizing committees, and as a Track/Session Chair for over 50 international conferences. He was a recipient of the 2010 Special Service Award from the IEEE Broadcast Technology Society. He is an IEEE BTS Distinguished Lecturer from 2012 to 2014.

Yao Zhao (M'06–SM'12) received the B.S. degree from Fuzhou University, Fuzhou, China, in 1989, and the M.E. degree from Southeast University, Nanjing, China, in 1992, both from the Radio Engineering Department, and the Ph.D. degree from the Institute of Information Science, Beijing Jiaotong University (BJTU), Beijing, China, in 1996.

He became an Associate Professor at BJTU in 1998 and became a Professor in 2001. From 2001 to 2002, he has been working as a Senior Research Fellow at the Information and Communication Theory Group, Faculty of Information Technology and Systems, Delft University of Technology, Delft, The Netherlands. He is currently the Director of the Institute of Information Science, BJTU. He is leading several national research projects from 973 Program, 863 Program, the National Science Foundation of China. His current research interests include image/video coding, digital watermarking, and content-based image retrieval.

Dr. Zhao was a recipient of the National Science Foundation of China for Distinguished Young Scholars in 2010.

Huihui Bai received the Ph.D. degree in signal and information processing from Beijing Jiaotong University (BJTU), Beijing, China, in 2008.

She is currently an Associate Professor with the Institute of Information Science, BJTU. She has been engaged in research and development work in video coding technologies and standards such as multiple description video coding and distributed video coding.

Dr. Bai is leading or participating in several research projects, such as the 973 Program, and the 863 Program, the National Natural Science Foundation of China.

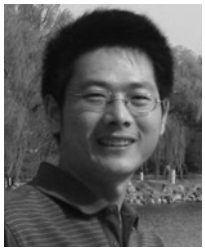

Huawei Tian received the B.E. degree in college of computer science of Chongqing University, Chongqing, China, in 2006. He is currently pursuing the Ph.D. degree at the Institute of Information Science, BJTU.

His current research interests include image processing, pattern recognition, digital watermarking and steganography, digital forensics, 3-D videos, and visual attention.